Energy Advances

ROYAL SOCIETY OF CHEMISTRY

PAPER

View Article Online
View Journal | View Issue

Cite this: *Energy Adv.*, 2024, 3, 574

A redox acceptor–acceptor nitro functionalized naphthalene diimide/rGO anode for sustainable lithium-ion batteries†

Madan R. Biradar,‡[ab] Nitish Kumar, ‡[cd] Prakash Kumar Pathak, ‡[c] Sidhanath V. Bhosale, *[ab] Sheshanath V. Bhosale *[e] and Rahul R. Salunkhe *[c]

Received 19th November 2023,
Accepted 12th January 2024

DOI: 10.1039/d3ya00561e

rsc.li/energy-advances

Organic materials capable of undergoing oxidation and reduction reactions are attracting attention as potential electrode components, providing a more environmentally sustainable alternative for lithium-ion batteries (LIBs). Despite notable achievements at the laboratory level, these materials still face challenges, such as high solubility in electrolyte solutions and limited thermal stability, leading to capacity degradation. While carbon remains the benchmark for anode materials, issues like irreversible capacity loss and low specific capacity impede the development of advanced LIBs. This study presents a composite material incorporating naphthalene diimide nitro derivatives (NDI-$2NO_2$ and NDI-$4NO_2$) into reduced graphene oxide (rGO) as an anode material for LIBs. The inclusion of rGO not only addresses the problem of material dissolution in the organic electrolyte, but also significantly improves the rate performance and conductivity of the resulting composite materials. Specifically, at a current density of 50 mA g^{-1}, the NDI-$4NO_2$/rGO composite demonstrates a remarkably high specific capacity of 699 mA h g^{-1}, while the NDI-$2NO_2$/rGO composite yields a specific capacity of approximately 560 mA h g^{-1}. Finally, we showcase that optimal performance as superior anode materials can be achieved by effectively combining organic compounds capable of participating in oxidation and reduction reactions with graphene-based composites.

Introduction

The rapid increase in the grid integration of renewable energy sources and the electric vehicle (EV) market has triggered demand for multi-terawatt-hour scale energy storage with low-cost, high-energy density, and safety in operation. The cost of lithium-ion battery (LIB) materials, geopolitical complexities associated with sourcing, and challenges concerning handling and recycling have prompted significant efforts in exploring alternatives.[1] On the other hand, the potential of organic electrode materials for electrochemical energy storage applications is highly regarded due to their advantageous properties, like abundant availability of constituent elements, sustainability, low cost, and minimal environmental impact.[2–4] Organic electrode materials offer a viable alternative for LIBs.[5–7] Considering the advantages of organic materials, extensive research has been carried out to develop both anode[8] and cathode[9] materials for LIBs. However, organic LIBs have underperformed, possessing significant drawbacks such as poor conductivity and reaction kinetics, low energy density, and high electrolyte solubility.[10–12]

Moreover, research efforts have been dedicated to discovering sustainable alternatives to conventional graphite anodes[13–15] that offer improved energy and power density. As a result, a wide range of alloy-based materials (such as Sn, P, Ge, Si, Bi, and Sb) and transition metal oxides (including M_xO_y, where M represents Ni, Mn, Fe, Cr, Mo, Co, Nb, *etc.*) have been extensively investigated as potential anode materials for LIBs, thanks to their high specific capacity.[16–18] However, these materials' electrochemical instability and rapid capacity degradation hinder their widespread commercial application as anode materials in LIBs. For example, silicon anodes can offer ten times the capacity of graphite (3580 mA h g^{-1}). However, the severe volumetric change (300–400%) during the lithiation causes mechanical failure and instability of the solid electrolyte

[a] *Polymers and Functional Materials Division, CSIR-Indian Institute of Chemical Technology, Hyderabad-500007, Telangana, India. E-mail: bhosale@iict.res.in*
[b] *Academy of Scientific and Innovative Research (AcSIR), Ghaziabad-201002, Uttar Pradesh, India*
[c] *Materials Research Laboratory, Department of Physics, Indian Institute of Technology Jammu, Jagti, NH-44, PO Nagrota, Jammu, J&K, 181221, India. E-mail: rahul.salunkhe@iitjammu.ac.in*
[d] *Department of Industrial and Materials Science, Chalmers University of Technology, Göteborg, SE-412 96, Sweden*
[e] *Department of Chemistry, School of Chemical Sciences, Central University of Karnataka, Kalaburagi-585 367, Karnataka, India. E-mail: bsheshanath@gmail.com*

† Electronic supplementary information (ESI) available. See DOI: https://doi.org/10.1039/d3ya00561e

‡ These authors contributed equally to this work.

interface (SEI) layer.[19,20] On the contrary, transition metal oxide anodes possess high capacity (600–1000 mA h g^{-1}) but have low coulombic efficiency and large potential hysteresis.[21,22] Transition metal chalcogenides are another interesting anode material with high theoretical capacity. However, the significant alterations in the bulk material dimensions during charging/discharging generally hamper their poor cycling stability and rate capabilities.[23,24] Conversely, MXenes, an emerging class of materials, have also been utilized as the anode. The low specific capacity and restacking characteristics of MXenes has limited their practical application in LIBs.[25,26] Most of these drawbacks of different materials can be addressed systematically by compositing them with carbon materials, including carbon nanotubes, reduced graphene oxide (rGO), and other porous carbon materials.[20,21] For example, including the carbon matrix into the silicon effectively managed the volumetric variations of silicon while preserving the electrodes' structural integrity and electrical stability.[27,28] Although, after a significant advancement in the anode materials, most of these materials employed in commercial LIBs rely on graphite materials having limited capacity (about 300 mA h g^{-1}) for commercial applications.[29,30]

Up to now, the redox-active organic electrode materials,[31] conducting polymers,[32,33] and organic carbonyl compounds[34] have been widely employed as anode materials in rechargeable LIBs.[1,35] To avoid unwanted dissolution of organic materials in the electrolyte solution, strategies such as designing and constructing molecular architectures with stable and redox-dependent functional groups have been previously adopted.[1,32–37] Different organic materials, including dilithium terephthalate and diethyl terephthalate,[38] Li-salt derived from 1,2,4-benzene tricarboxylic acid,[39] and organic compounds with nitro-containing groups like 2,2′-azobis(2-methyl propionitrile) and 2,2′-azobis(2-methylpropionamidine)dihydrochloride[40] have been utilized in the literature. The key challenges associated with these molecules are the low-capacity values and their lower cycling stability.

Furthermore, to address this issue, different organic molecules utilizing bare naphthalene diimides (NDIs) and their composites have been reported in the literature,[41–46] as shown in Fig. 1(a)–(g). NDIs are π-conjugated aromatic molecular chromophores bearing n-type semiconducting properties.[47] Their ease of structural modification, thermal stability, and ability to incorporate redox-active functional groups,[48] and to accept electrons are beneficial to tune the material properties. Towards this effort, Vadehra *et al.*[46] reported the importance of various core substitutions on NDI molecules and their effect on the redox potential window. Furthermore, Stoddart and co-workers[44] reported the rigidity of the NDI molecule and its effect on the cathodic properties for LIBs. Also, different nitro organic compounds were utilized as a cathodic electrode material in LIBs to enhance the potential window.[49] Ye *et al.* recently

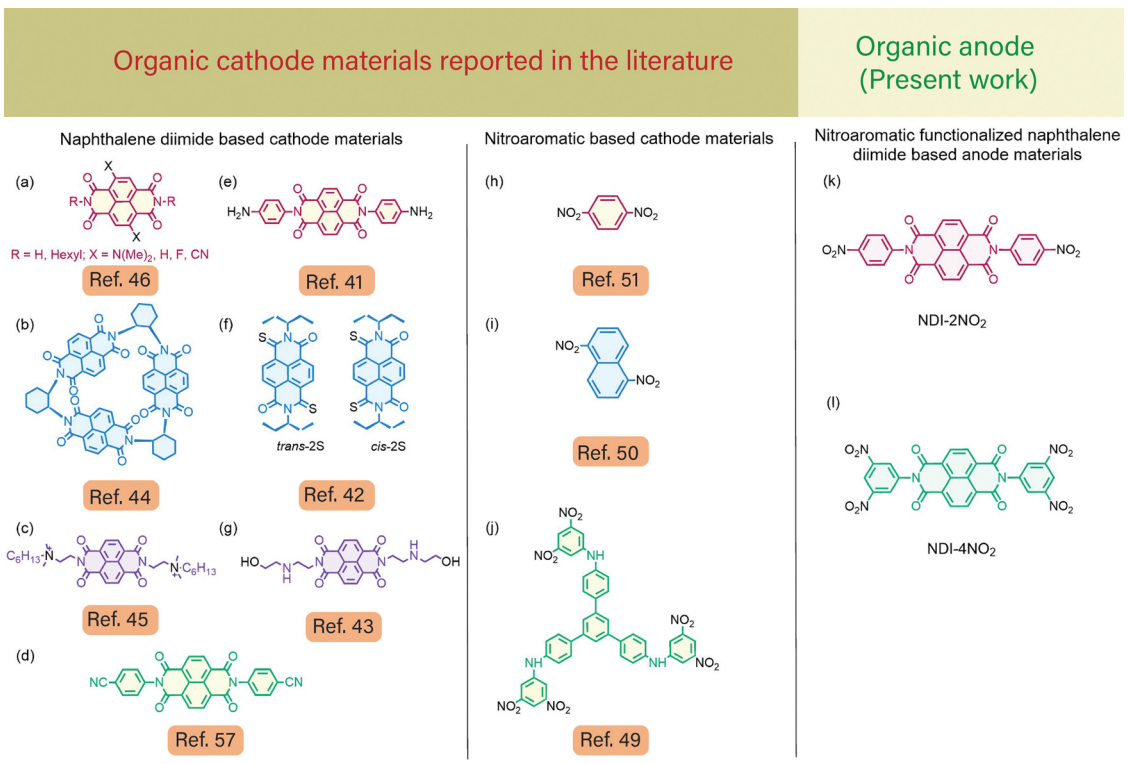

Fig. 1 Various cathodes reported in the literature (corresponding specific capacity and average potential V *vs.* Li^+/Li). (a) *N*-hexyl-nitrile-substituted NDI 9 (105 mA h g^{-1}@0.2C, 2.8 V), (b) (−)-NDI-Δ (150 mA h g^{-1}@0.1C, 2.5 V), (c) NDI–rGO (200 mA h g^{-1}@25 mA g^{-1}, 2.4 V), (d) NDI-CN, (e) naphthalenediimide diamine (240 mA h g^{-1}@50 mA g^{-1}, 2.1 V), (f) P-NDI *trans*-2S and *cis*-2S (120 mA h g^{-1}@50 mA g^{-1}, 2.40 V), (g) NDI-NHOH (122 mA h g^{-1}@0.05C, 2.36 V), (h) p-DNB (535 mA h g^{-1}@50 mA g^{-1}, 2.67 V), (i) 1,5-DNN (1338 mA h g^{-1}@20 mA g^{-1}, 2.45 V), and (j) TAPB-6NO_2 (120 mA h g^{-1}@50 mA g^{-1}, 2.0 V). (a)–(g) Naphthalene diimide-based small molecules as cathode materials, (h)–(j) nitroaromatic compounds as cathode materials, and (k) and (l) nitroaromatic functionalized NDIs as anode materials reported in the present work.

explored *p*-, *o*-, and *m*-dinitrobenzene (DNB) compounds as cathode materials in LIBs.[50] For as-fabricated LIBs, they observed that *p*-dinitrobenzene exhibited a reversible capacity of 535 mA h g^{-1} at 50 mA g^{-1} (average potential of 2.7 V). However, due to the high solubility of organic scaffolds, such as *p*-DNB, the capacity of LIBs gradually dropped to 54% after 50 cycles. Recently, Zhang *et al.* reported an organic cathode material based on nitro compounds.[49] They demonstrated that incorporating multiple nitro-functional groups in organic molecular architectures efficiently reduced the solubility in the electrolyte solution and exhibited a high specific capacity of about 180 mA h g^{-1}.

Fig. 1(h)–(j) show different nitroaromatics reported in the literature.[49,50] Although NDIs[41,43,45–48] and nitroaromatic[49–51] based small molecular cathode materials in LIBs show significant advantages with a high specific capacity, there are no reports available in the literature about the use of NDI-nitroaromatics and rGO nanocomposites as anodes in LIBs.

The inherent properties of NDI molecules, such as their ability to undergo π–π aromatic stacking, make them highly suitable for electron transfer and diverse design architecture, rendering them ideal candidates for LIBs. In order to further enhance their electrochemical properties, we have introduced nitro substitutions on the NDI moieties, specifically NDI-$2NO_2$ and NDI-$4NO_2$. One of the challenges faced in utilizing organic materials in LIBs is their tendency to dissolve in the electrolyte.[50] To address this issue, we have proposed immobilizing organic materials onto solid substrates, which offers a feasible solution to overcome the dissolution problem. Our research successfully incorporated NDI-$2NO_2$ and NDI-$4NO_2$ with rGO through non-covalent interactions. The π–π interaction between NDI and rGO further enhances the material's suitability for LIBs. Additionally, electron-withdrawing nitro groups appended on the NDI ring increase the electron-deficient nature, whereas rGO also serves as an electron acceptor.[45] These combined characteristics make our approach scientifically sound and promising for developing high-performance LIBs.

Here, we report the LIB performance from rGO with NDI-phenyl dinitro (NDI-$2NO_2$) and NDI-phenyl tetra-nitro (NDI-$4NO_2$), organic architectures fabricated from NDI, *p*-nitro aniline (*p*NA) and 3,5-meta-dinitro aniline (3,5-*d*NA), respectively. The NDI-$4NO_2$/rGO sample exhibited a high specific capacity of about 699 mA h g^{-1} at 50 mA g^{-1}. In addition, the material shows an outstanding cycling stability of 800 cycles with minimal fading. Our investigation has explored the redox mechanism of NDI-$2NO_2$/rGO and NDI-$4NO_2$/rGO and the potential of incorporating nitroaromatic functional groups into NDI compounds to develop better anode materials for LIBs.

Results and discussion

Characterization of the NDI-$2NO_2$ and NDI-$4NO_2$ molecules

The synthesized compounds' structures were confirmed using different spectroscopic techniques (Fig. S1–S5, ESI†). FTIR analysis was performed by a PerkinElmer spectrum (Spectrum 100; PerkinElmer). The comparative FTIR spectra of the NDI-$2NO_2$ and NDI-$4NO_2$ molecules confirm the appearance of functional groups like aromatic H–C═C (3081, 3088 cm^{-1}), –C═O (1714 cm^{-1}), –C═C (1580, 1536 cm^{-1}), *etc.* (Fig. S1, ESI†). Furthermore, ^{1}H NMR spectra of NDI-$4NO_2$ showed the presence of a proton peak designated as 'a' at 9.01 (m, 2H); additionally, a proton peak labelled as 'b' appeared at 8.96 (d, 4H), and another proton peak labelled as 'c' emerged at 8.82 (s, 4H) (Fig. S2, ESI†). Similarly, ^{1}H NMR spectra of NDI-$2NO_2$ showed the appearance of an 'a' labelled proton peak at 8.76 (s, 4H) and 'b' labelled proton peak at 8.47–8.44 (d, 4H), and a proton peak labelled as 'c' appeared at 7.83–7.81 (dd, 4H), as displayed in Fig. S3 (ESI†), which confirmed the formation of NDI-$2NO_2$ and NDI-$4NO_2$ molecules. Furthermore, the HRMS spectrum of NDI-$4NO_2$ indicates a good agreement between the *m*/*z* calculated for $C_{26}H_{12}O_8N_4$: 598.03512, and the experimental value: $[M]^+$ 598.03400 (Fig. S4, ESI†). Similarly, the HRMS spectrum of NDI-$2NO_2$ indicated a good agreement between the calculated and experimental values (Fig. S5 (ESI†); *m*/*z* $[M]^+$ calculated for $C_{26}H_{12}O_8N_4$: 508.06536, experimental: 508.06496). The as-prepared organic molecules were soluble in organic solvents, making it difficult to use them as the anode material in the presence of organic electrolytes. Hence, they have been composited with rGO. The self-assembled composite formation with rGO is a practical design strategy to suppress the dissolution of NDI derivatives in organic electrolytes.[52] During the composite formation, the interaction between NDI and rGO may enhance the electron transfer rate, impacting the composite material's high cycling stability, similar to the previous report.[53] Notably, the functional groups such as C═O, C═C and C–O–H in rGO can be advantageous for binding with organic materials.

The schematic representation of the synthesis process for NDI-$4NO_2$/rGO and NDI-$2NO_2$/rGO materials is shown in Scheme 1. Co-precipitation of NDI-$2NO_2$, NDI-$4NO_2$, and graphene oxide (GO) was utilized for obtaining composite materials. Hydrazine hydrate (NH_2NH_2) helped reduce GO to rGO. Further details of the synthesis process can be found in the Experimental section and Note S1 (ESI†). The thermal stability of rGO, NDI-$2NO_2$/rGO, and NDI-$4NO_2$/rGO under a nitrogen environment was determined using thermogravimetric analysis (TGA). Measurement was performed using a TA instrument Q500 TGA under flowing nitrogen gas at a heating rate of 10° min^{-1} up to 800 °C. As shown in Fig. S6 (ESI†), the TGA results reveal that bare rGO, NDI-$2NO_2$/rGO, and NDI-$4NO_2$/rGO displayed 5% water loss between temperatures of approximately 300 °C due to thermal decomposition. These TGA results suggest that the composites NDI-$2NO_2$/rGO and NDI-$4NO_2$/rGO are thermally stable and can be utilized for energy storage applications.

Structural studies

Detailed structural investigations were carried out for different samples, as shown in Fig. 2. FTIR was employed to examine the reduction of GO to rGO and the formation of composite materials NDI-$2NO_2$/rGO and NDI-$4NO_2$/rGO (Fig. 2a). The

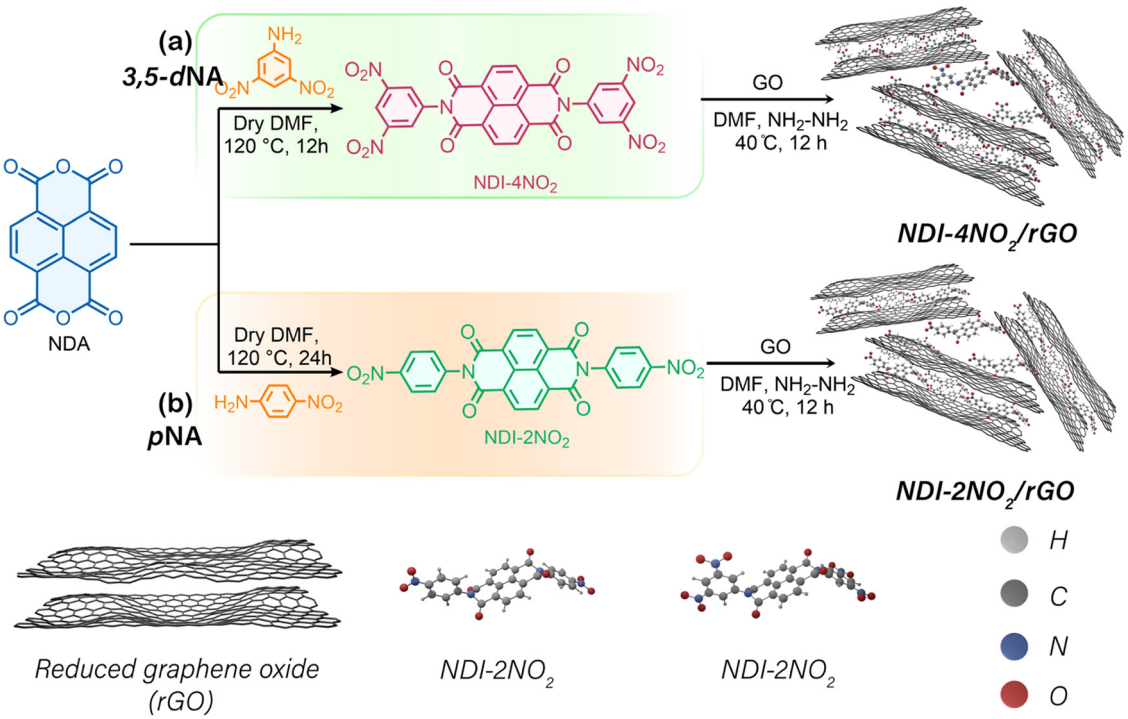

Scheme 1 Schematic for synthesizing the NDI-$2NO_2$/rGO and NDI-$4NO_2$/rGO composite materials.

peaks around 3700 cm^{-1} are attributed to the –OH stretching vibrations. This may yield from the adsorbed water content in the samples.[54] Additionally, rGO exhibits the characteristic peaks at 1711, 1556, and 1181 cm^{-1} corresponding to the C═O, C═C, and C–O–H stretching vibrations.[55] The FTIR spectra of NDI-$2NO_2$/rGO exhibited peaks of about 1700 cm^{-1} attributed to the stretching vibration of the imide C═O group. Moreover, the two peaks at 1565 and 1412 cm^{-1} correspond to the stretching vibrations of the –NO_2 functional group.[50] The peaks that appeared at 870 and 755 cm^{-1} can be ascribed to the C–H bending vibrations.[56] The presence of peaks at 1644, 1412, and 1242 cm^{-1} was attributed to C═O, C═C and C–O–H bonding in the rGO in the sample.[57] Similar peaks were observed in the NDI-$4NO_2$/rGO sample. Thus, the comprehensive FTIR study confirmed the successful synthesis of composite materials. Moreover, UV-vis absorption studies were performed on a UV-vis-1800 Shimadzu spectrometer, and the results are depicted in Fig. 2b. The sample rGO showed an intense absorption peak at 270 nm,[57] while there is a small absorption peak for NDI-$2NO_2$ at 264 nm (imide substituted phenyl ring system), along with one shoulder peak at 338 nm and two intense peaks at 356 and 377 nm.[57] The absorption peaks ranging from 300 to 400 nm are typical of the NDI subunits and are unaffected by imide substitution.[58] The NDI-$4NO_2$ molecular architecture showed an intense absorption peak at 268 nm (phenyl ring system) and a broad peak ranging from 330 nm to 370 nm corresponding to the NDI core. Moreover, the absorption curves of the NDI-$2NO_2$/rGO and NDI-$4NO_2$/rGO composites exhibited peaks at 269 nm, 338 nm (shoulder), and two intense peaks at 356 nm and 377 nm, suggesting the complex formation. The intense peak at 269 nm (due to π–π transition) is the characteristic graphene peak indicating the presence of rGO in the NDI-$2NO_2$/rGO and NDI-$4NO_2$/rGO composites.[59] Furthermore, the organic molecule's composition with rGO was investigated using Raman spectroscopy on the Horiba Jobin–Yvon Lab Ram HR spectrometer with an excitation wavelength of 632.8 nm. Fig. 2c shows that different samples exhibited characteristic peaks at 1333 and 1600 cm^{-1}, corresponding to the D and G bands.[60] The I_D/I_G ratio for the bare rGO sample was calculated to be 1.4, which increased to 1.44 for NDI-$2NO_2$/rGO and 1.24 for the NDI-$4NO_2$/rGO samples, respectively. The decreased I_D/I_G ratio indicates a higher degree of graphitization for the NDI-$4NO_2$/rGO sample.[61] The crystallographic structures of the rGO, NDI-$2NO_2$/rGO, and NDI-$4NO_2$/rGO composites are further verified by powder X-ray diffraction (P-XRD) measurements recorded on a Bruker AXS D8 (λ = 1.54 Å), and the results are depicted in Fig. S7 (ESI†). The bare rGO sample exhibited two diffraction peaks around 25° and 44°, corresponding to the standard graphite 2H phase. The composite NDI-$2NO_2$/rGO exhibited four peaks around 13, 26.5, 29.5, and 43.5, whereas NDI-$4NO_2$/rGO displayed peaks at about 12.8, 26.4, and 43 degrees.[62] The composites NDI-$2NO_2$/rGO and NDI-$4NO_2$/rGO exhibited higher crystallinity than rGO, indicated by the sharp and enhanced peaks. The diffraction peaks moving towards high angles indicate that the π–π stacking between NDI moieties, such as NDI-$2NO_2$ and NDI-$4NO_2$, and the rGO surface was enhanced.[63]

Furthermore, the elemental content and the bonding conditions of the NDI-$2NO_2$/rGO and NDI-$4NO_2$/rGO composites were examined by X-ray photoelectron spectroscopy (XPS)

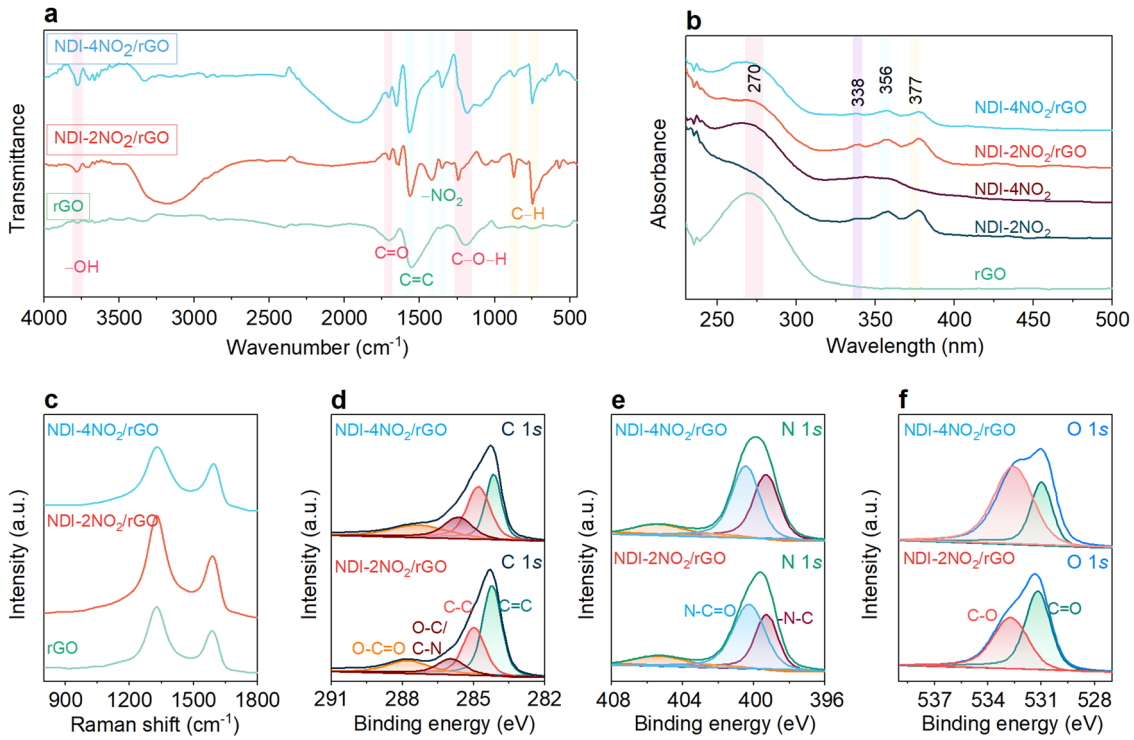

Fig. 2 Structural characterization of the composite materials using spectroscopic and X-ray techniques. (a) Comparative FT-IR spectra of rGO, NDI-4NO_2/rGO, and NDI-2NO_2/rGO; and (b) UV-vis spectra of different samples. (c) Stacked Raman spectra of rGO, NDI-2NO_2/rGO, and NDI-4NO_2/rGO, showing the presence of D and G bands. Comparative high-resolution XPS spectra for NDI-2NO_2/rGO and NDI-4NO_2/rGO of the (d) C 1s region, (e) N 1s region, and (f) O 1s region.

measurements (Model Nexa from Thermofisher Scientific). The XPS survey spectra displayed in Fig. S8 (ESI†) exhibit the presence of carbon (C), oxygen (O), and nitrogen (N) elements only. The high-resolution narrow region spectra for various samples are shown in Fig. 2d–f. The deconvoluted spectra for the C 1s spectrum of NDI-2NO_2/rGO and NDI-4NO_2/rGO (Fig. 2d) can be fitted into four types of peaks located at 287.3 eV (O–C═O), oxygen and nitrogen bridged carbon (O–C and C–N) at 285.6 eV, carbon bridged carbon (C–C) at 284.8 eV and graphitic carbon (C═C) at 284.2 eV.[64] Also, the high-resolution N 1s XPS spectrum for both composite samples (Fig. 2e) is dominated by two well-resolved peaks at 400.3 eV and 399.2 eV, corresponding to N–C═O and –N–C, respectively.[65] Moreover, the O 1s spectrum of NDI-4NO_2/rGO could be divided into two fitting peaks at 533.6 eV and 531 eV corresponding to carbon bridged oxygen C–O bonds and C═O bonds, respectively.[60] Similar peaks were also confirmed for the NDI-2NO_2/rGO sample (Fig. 2f). The XPS results of the NDI-2NO_2/rGO and NDI-4NO_2/rGO composites revealed that the nitrogen and oxygen content of the nitro functional groups dominated the composite. Tables S1 and S2 (ESI†) show the atomic percentage of C, N and O for NDI-2NO_2/rGO and NDI-4NO_2/rGO, which aligns with the EDS data.

Morphological studies

The morphology of the as-prepared NDI-2NO_2/rGO and NDI-4NO_2/rGO composites was investigated using the field emission scanning electron microscopy (FE-SEM) technique using JEOL JSM 7900F machine. The sheet-like morphology was confirmed for both composite samples, as displayed in Fig. S9a–d (ESI†). These FESEM images confirm the composition with rGO as these organic molecules tend to grow over the rGO sheets. Furthermore, the chemical composition of the as-prepared NDI-2NO_2/rGO and NDI-4NO_2/rGO composites was characterized by energy-dispersive X-ray spectroscopy (EDS, Fig. S10, ESI†). The EDS spectra depict the presence of C, N, and O elements in both NDI-2NO_2/rGO and NDI-4NO_2/rGO, and their atomic percentage is tabulated in the inset of Fig. S10 (ESI†). The EDS elemental mappings further confirmed various elements' uniform distribution, as shown in Fig. S11 (ESI†). The NDI-4NO_2/rGO composite showed higher nitrogen content than the NDI-2NO_2/rGO composite. The increased nitrogen content in the molecular architecture was also proved by both XPS and EDS mapping (Tables S1, S2 and Fig. S10, ESI†). Thus, an increase in nitro-functional groups might be useful for controlling the solubility issue of organic molecules.

The N_2 adsorption/desorption isotherm was performed at 77 K to further investigate the surface area and pore size distribution. The analysis was performed on an Autosorb-iQ (Quantachrome) at 77 K. The comparative isotherms for both materials are shown in Fig. S12 (ESI†). The steep adsorption isotherm at the low-pressure region of both composites was observed, indicating the typical type IV behavior.[66] The estimated Brunauer–Emmett–Teller (BET) surface area of the NDI-

$2NO_2$/rGO and NDI-$4NO_2$/rGO composite is 34.7 m^2 g^{-1} and 41.1 m^2 g^{-1}, respectively. The average pore diameter for NDI-$2NO_2$/rGO and NDI-$4NO_2$/rGO was observed to be 3.2 nm and 3.0 nm, respectively (Fig. S12b and d, ESI†). Thus, it confirms the presence of various pores in these materials. The BET surface area, pore diameter, and pore volume of NDI-$4NO_2$/rGO are higher than that of NDI-$2NO_2$/rGO, indicating that the former composite may provide comparatively good electrochemical performance.

Electrochemical testing

The electrochemical performance was investigated using cyclic voltammetry (CV), galvanostatic charge–discharge (GCD) profiles, and electrochemical impedance spectroscopy (EIS). The CV and EIS were performed on a Biologic VSP electrochemical workstation while charging–discharging measurements were taken on a potentiostat Neware battery tester. The CV was observed at a scan rate of 0.2 mV s^{-1} within a stable voltage window of 0–3 V, as shown in Fig. 3a. During the cathodic sweep, the peak at 0.01 V shows the typical lithiation process, while the anodic peaks at 0.25 V and 1.75 V correspond to delithiation.[67] A comparative CV plot shows that NDI-$4NO_2$/rGO encloses a larger CV area than NDI-$2NO_2$/rGO, implying the high electrochemical activity of the sample, suitable to facilitate more charge storage and competent for LIB anodes. Furthermore, the materials were subjected to GCD tests, as shown in Fig. 3b. The NDI-$4NO_2$/rGO exhibits a high specific capacity of 699 mA h g^{-1} at a current rate of 50 mA g^{-1} with the average potential of lithium insertion at 0.41 V (as per eqn (1) mentioned in Note S2, ESI†). The cell was kept at open circuit potential for 24 hours to study the self-discharge after lithiation. A negligible voltage drop was observed for a long period (Fig. S13, ESI†), indicating good stability of our anodic material. The NDI-$4NO_2$/rGO outperforms various previously reported organic materials such as G@PI/rGO (198 mA h g^{-1}@ 30 mA g^{-1}),[68] DP-NTCDI-250 (170 mA h g^{-1}@25 mA g^{-1}),[69] and NDIDA-GO (240 mA h g^{-1}@50 mA g^{-1}).[41] The reason for the outstanding performance of NDI-$4NO_2$/rGO is the high nitrogen content contributed by four nitro groups from the sample. In the case of NDI-$2NO_2$/rGO, two nitro groups are

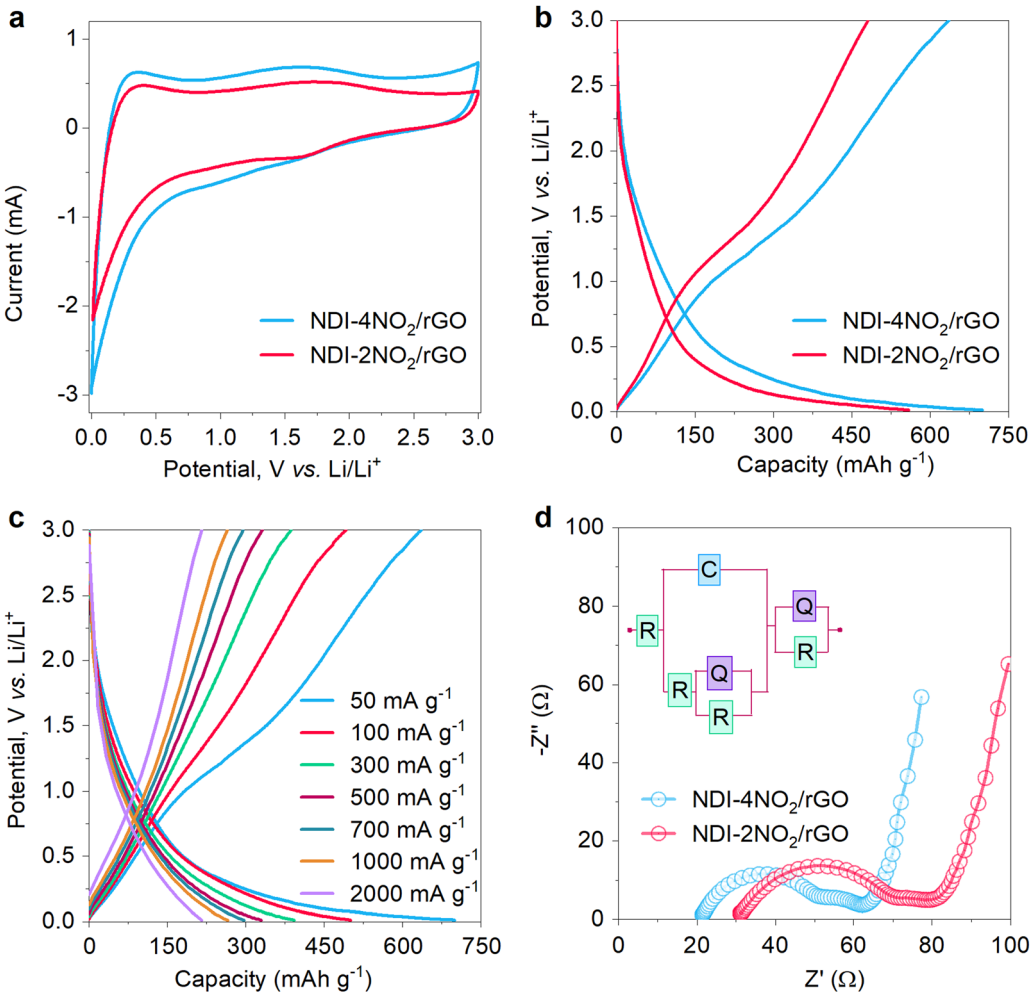

Fig. 3 Electrochemical data for LIB half-cell studies. (a) Comparative CV for the NDI-$2NO_2$/rGO and NDI-$4NO_2$/rGO samples. (b) The first charge–discharge curve profile at a current density of 50 mA h g^{-1} for both samples, (c) the charge–discharge curves of the NDI-$4NO_2$/rGO sample at current densities varying from 50 to 2000 mA h g^{-1}. (d) The comparative Nyquist plots for the NDI-$2NO_2$/rGO and NDI-$4NO_2$/rGO samples.

involved in the redox reaction. This nitro group enables improved electric conductivity required for faster kinetics of electrons and provides extra sites for more lithium storage.[70] Also, nitroaromatic compounds facilitate six electrons during redox reactions in LIBs, benefiting the charge storage ability. Thus, NDI-4NO_2/rGO showed a multi-electron reaction per active group, which impacted the specific capacity.[36,37] The NDI-4NO_2/rGO were further subjected to perform GCD at various current densities, ranging from 100 to 2000 mA g^{-1}. The material exhibits specific capacities of 498, 389, 325, 296, 263 and 216 mA h g^{-1}, as shown in Fig. 3c. The electrochemical stability of the material at higher current densities shows a remarkable performance compared to various organic compounds, as shown in the comparative data in Table S3 (ESI†). The corresponding redox mechanism is discussed in Note S3 (ESI†).

The kinetics of Li^+ were investigated using EIS measurement by applying alternating current with an amplitude of 5 mV with frequency ranging from 10 mHz to 100 kHz. Fig. 3d shows a comparative Nyquist plot of the NDI-4NO_2/rGO and the NDI-2NO_2/rGO. The inset in Fig. 3d shows the simulated Randles circuit, which fits in with the experimental data. The NDI-4NO_2/rGO sample has less electrode resistance (21.3 Ω) than the NDI-2NO_2/rGO sample (31.1 Ω). Also, the charge transfer resistances (R_{ct}) of NDI-4NO_2/rGO and NDI-2NO_2/rGO are 36.2 Ω and 45.3 Ω, which reveals a low resistance path for Li^+ ions in the NDI-4NO_2/rGO sample. The CV and EIS were conducted for bare rGO for comparison shown in Fig. S14 (ESI†), which reveals that the R_{ct} of rGO is 7.2 Ω, contributing to the high conductivity and low resistance path for the NDI samples.

The LIB coin cell composed of NDI-4NO_2/rGO was further evaluated by capacity retention tests, and cyclability and diffusion studies. For the capacity retention test, current rates ranging from 50 to 5000 mA g^{-1} were applied and the specific capacities are shown in Fig. 4a. The cell shows some electrochemical changes during the first cycles, which gives a stable performance. The LIB cells composed of NDI-4NO_2/rGO exhibited specific discharge capacities of 699, 498, 389, 325, 296, 263, 216 and 155 at current rates of 50, 100, 300, 500, 700, 1000, 2000 and 5000 mA g^{-1}, respectively. The cell exhibits a stable performance at low as well as high current. Furthermore, the cyclability of the cells was tested for 800 cycles at a current rate of 1000 mA g^{-1}; the device has demonstrated excellent stability, retaining about 89% of its initial

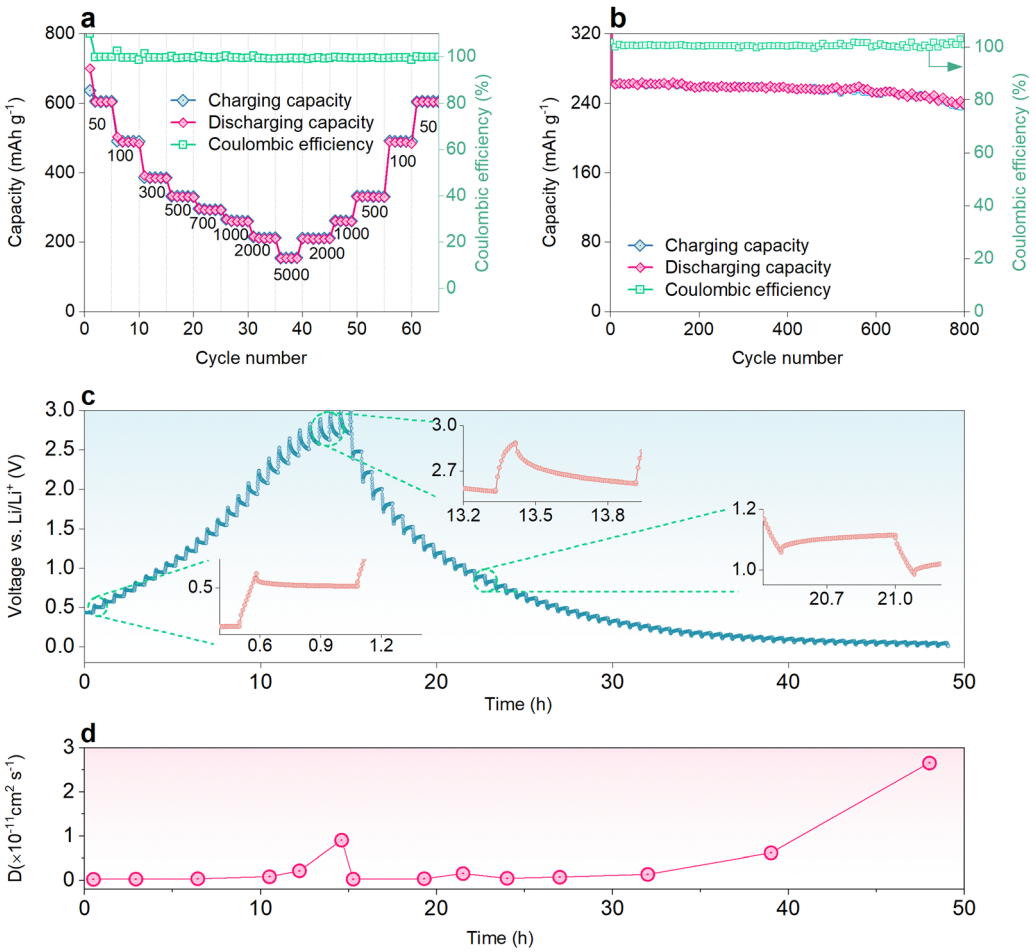

Fig. 4 Extended electrochemical performance testing. (a) Capacity retention at different current densities. (b) Cycling stability test showing the steady performance of the anode up to 800 cycles at 1000 mA g^{-1}, (c) GITT charge–discharge curve with a resting period of 30 min. The insets show the zoomed-in pulse profiles at various charging/discharging stages, and (d) the diffusion coefficient at different charge/discharge stages.

capacity, as shown in Fig. 4b. The coulombic efficiency of the LIB cell was above 95% throughout the cycling, revealing very low hysteresis during charge–discharge. To present a comparative analysis of the NDI-2NO_2/rGO LIB cell, its cycling tests were conducted for 500 cycles at 1000 mA g^{-1}, which retained about 74% of its initial capacity. One of the reasons which govern the outstanding performance of NDI-4NO_2/rGO is the increased nitrogen content, specifically the pyridinic type (as discussed in the XPS Characterization section) content with the highly π-conjugated structure and higher specific surface area.[71]

The diffusion study of Li^+ ions into the host materials was studied using the galvanostatic intermittent titration technique (GITT). During the study, the charge–discharge pulse of 10 min was applied, followed by a resting period of 30 min. The diffusion coefficient (D) was calculated by eqn (2), Note S2 (ESI†). The GITT charge–discharge profile and corresponding D values are plotted as a function of time, as shown in Fig. 4c and d. During the charging, the D value increases from 2.6×10^{-13} cm^2 s^{-1} to 1.01×10^{-11} cm^2 s^{-1}.

In contrast, during discharging, the D value is constant when it is above 0.5 V. Still, it increases rapidly in the region when the discharge curve is below 0.5 V. The high value of D manifests the fast diffusion of Li^+ ions into the host material. Hence, these electrochemical studies show that the NDI-4NO_2/rGO can be successfully employed as an anode material for LIBs. Along with the superior anodic performance, this cost-effectiveness, greener synthesis route of this material, and its non-solubility within electrolyte, give an upper hand over various traditional organic materials, as listed in Table S3 (ESI†).

Conclusions

In conclusion, we synthesized NDI-nitro derivatives using *p*NA and 3,5-*d*NA appended on electron acceptor NDI molecules. The synthesized NDI-2NO_2 and NDI-4NO_2 molecules are further grafted on reduced graphene oxide by non-covalent interactions, which are investigated for LIB applications. The NDI-4NO_2/rGO showed a specific capacity of 699 mA h g^{-1}, while the NDI-2NO_2/rGO sample showed only 560 mA h g^{-1} at a current density of 50 mA g^{-1}. Furthermore, we performed a cycling stability study of NDI-4NO_2/rGO for 800 cycles; it retained 89% initial capacity, whereas NDI-2NO_2/rGO showed 74% initial capacity retention after 500 cycles. The excellent electrochemical performance of NDI-4NO_2/rGO is due to the highly π-conjugated NDI-4NO_2 structure, increased nitrogen contents, electrolyte insolubility, and fast redox kinetics. The enhanced conductivity of the NDI-4NO_2/rGO composite material is due to non-covalent interaction with reduced graphene oxide. Furthermore, the versatility of molecular engineering will allow us to tune the performance of organic molecules to enhance the performance, such as capacity and stability, towards practical organic batteries.

Experimental section

The material syntheses of NDI-2NO_2, NDI-4NO_2 and graphene oxide (GO) are discussed in Note S1 in detail (ESI†).

Synthesis of the NDI-2NO_2/rGO composite and NDI-4NO_2/rGO composite

NDI-2NO_2 and NDI-4NO_2 can be synthesized in a single step through the reaction of NDA with *p*NA and 3,5-*d*NA in dimethylformamide (DMF) at 120 °C for 12 and 24 h, respectively. The reactivity of NDA with nitro-functionalized aniline is low due to the electron-withdrawing effect of the nitro group on the aromatic ring system. Consequently, a longer reaction time is required to produce NDI-4NO_2 than NDI-2NO_2.[45]

Electrode preparation and cell packing

The methodology of slurry preparation and coating is as per our earlier reports.[72] The powder samples of NDI-2NO_2/rGO and NDI-4NO_2/rGO (80%) were mixed with PVDF (10%) and carbon black super-P (10%) and hand-crushed for 30 min with the help of a pestle and mortar. This powder is then mixed in NMP solvent to prepare a slurry. The homogeneous slurry was coated over copper foils with the help of a tape casting coater with mass loading of about 1.2–1.6 mg and thickness of 50 μm, followed by drying under a vacuum at 80 °C. The coated foils were calendared for better material adhesion and crack-free electrode preparation. The 16 mm copper disks of the coated material were cut by a disk cutter and used as the active electrode for battery testing.

The coin cell (CR 2032) was packed by using the 16 mm active electrode disks, lithium chips (16 mm) as a counter electrode, Whatman filter paper of grade-1 as the separator, and $LiPF_6$ in EC : DMC (1 : 1) in the PC electrolyte. The cell was packed with the help of a crimper and kept at room temperature for 12 h for thermodynamic equilibrium attainment and proper electrolyte wettability.

Author contributions

The manuscript was written through the contributions of all authors. All authors have approved the final version of the manuscript. Madan R. Biradar, Nitish Kumar and Prakash Kumar Pathak contributed equally.

Conflicts of interest

There are no conflicts to declare.

Acknowledgements

S. V. B. (IICT) is thankful for financial support from CSIR-IICT (MS No. IICT/Pubs./2023/205). S. V. B. (GU) acknowledges the University Grant Commission (UGC) Faculty Research Program, New Delhi, India (F.4-5(50-FRP)(IV-Cycle)/2017(BSR)) for the award of a Professorship and also acknowledges Council of Scientific & Industrial Research (CSIR), India for providing support, code no. 02(0357)/19/EMR-II. M. R. B. is grateful for financial support through SRF from UGC, New Delhi. R. R. S. expresses gratitude to the SERB for the significant monetary assistance provided through the CRG/2020/003199 grants.

References

1 T. B. Schon, B. T. McAllister, P. F. Li and D. S. Seferos, *Chem. Soc. Rev.*, 2016, **45**, 6345–6404.
2 P. Poizot, J. Gaubicher, S. Renault, L. Dubois, Y. Liang and Y. Yao, *Chem. Rev.*, 2020, **120**, 6490–6557.
3 A. E. Lakraychi, F. Dolhem, A. Vlad and M. Becuwe, *Adv. Energy Mater.*, 2021, **11**, 2101562.
4 Y. Liang and Y. Yao, *Joule*, 2018, **2**, 1690–1706.
5 J. Wang, P. Apostol, D. Rambabu, X. Guo, X. Liu, K. Robeyns, M. Du, Y. Zhang, S. Pal, R. Markowski, F. Lucaccioni, A. E. Lakraychi, C. Morari, J. F. Gohy, D. Gupta and A. Vlad, *Sci. Adv.*, 2023, **9**, eadg607.
6 E. Pomerantseva, F. Bonaccorso, X. Feng, Y. Cui and Y. Gogotsi, *Science*, 2019, **366**, eaan8285.
7 M. Li, J. Lu, Z. Chen and K. Amine, *Adv. Mater.*, 2018, **30**, 1800561.
8 R. Guo, Y. Wang, S. Heng, G. Zhu, V. S. Battaglia and H. Zheng, *J. Power Sources*, 2019, **436**, 226848.
9 M. G. Mohamed, S. U. Sharma, C. H. Yang, M. M. Samy, A. A. K. Mohammed, S. V. Chaganti, J. T. Lee and S. Wei-Kuo, *ACS Appl. Energy Mater.*, 2021, **4**, 14628–14639.
10 S. Lee, G. Kwon, K. Ku, K. Yoon, S. Jung, H. Lim and K. Kang, *Adv. Mater.*, 2018, **30**, 1704682.
11 D. Xu, M. Liang, S. Qi, W. Sun, L. P. Lv, F. H. Du, B. Wang, S. Chen, Y. Wang and Y. Yu, *ACS Nano*, 2021, **15**, 47–80.
12 S. Lee, J. Hong and K. Kang, *Adv. Energy Mater.*, 2020, **10**, 2001445.
13 H. Zhang, Y. Yang, D. Ren, L. Wang and X. He, *Energy Storage Mater.*, 2021, **36**, 147–170.
14 C. Wang, C. Yang and Z. Zheng, *Adv. Sci.*, 2022, **9**, 2105213.
15 L. Zhao, B. Ding, X. Qin, Z. Wang, W. Lv, Y. He, Q. Yang and F. Kang, *Adv. Mater.*, 2022, **34**, 2106704.
16 S. Chae, M. Ko, K. Kim, K. Ahn and J. Cho, *Joule*, 2017, **1**, 47–60.
17 T. Sun, C. Liu, J. Wang, Q. Nian, Y. Feng, Y. Zhang, Z. Tao and J. Chen, *Nano Res.*, 2020, **13**, 676–683.
18 X. Wang, S. Tang, W. Guo, Y. Fu and A. Manthiram, *Mater. Today*, 2021, **50**, 259–275.
19 Y. Cui, *Nat. Energy*, 2021, **6**, 995–996.
20 P. U. Nzereogu, A. D. Omah, F. I. Ezema, E. I. Iwuoha and A. C. Nwanya, *Appl. Surf. Sci. Adv.*, 2022, **9**, 100233.
21 W. Qi, J. G. Shapter, Q. Wu, T. Yin, G. Gao and D. Cui, *J. Mater. Chem. A*, 2017, **5**, 19521–19540.
22 M. Zheng, H. Tang, L. Li, Q. Hu, L. Zhang, H. Xue and H. Pang, *Adv. Sci.*, 2018, **5**, 1700592.
23 B. Y. Guan, Y. Lu, Y. Wang, M. Wu and X. W. (David) Lou, *Adv. Funct. Mater.*, 2018, **28**, 1706738.
24 J. Dai, J. Li, Q. Zhang, M. Liao, T. Duan and W. Yao, *Mater. Lett.*, 2019, **236**, 483–486.
25 Q. Tang, Z. Zhou and P. Shen, *J. Am. Chem. Soc.*, 2012, **134**, 16909–16916.
26 K. A. Papadopoulou, A. Chroneos and S. R. G. Christopoulos, *J. Appl. Phys.*, 2023, **133**, 030901.
27 X. Zhang, D. Kong, X. Li and L. Zhi, *Adv. Funct. Mater.*, 2018, **29**, 1806061.
28 S. Chae, N. Kim, J. Ma, J. Cho and M. Ko, *Adv. Energy Mater.*, 2017, **7**, 1700071.
29 T. Kim, W. Song, D. Y. Son, L. K. Ono and Y. Qi, *J. Mater. Chem. A*, 2019, **7**, 2942–2964.
30 J. W. Choi and D. Aurbach, *Nat. Rev. Mater.*, 2016, **1**, 16013.
31 H. Wang, C. J. Yao, H. J. Nie, K. Z. Wang, Y. W. Zhong, P. Chen, S. Mei and Q. Zhang, *J. Mater. Chem. A*, 2020, **8**, 11906–11922.
32 Z. Xu, S. Hou, Z. Zhu, P. Zhou, L. Xue, H. Lin, J. Zhou and S. Zhuo, *Nanoscale*, 2021, **13**, 2673–2684.
33 S. Muench, A. Wild, C. Friebe, B. Häupler, T. Janoschka and U. S. Schubert, *Chem. Rev.*, 2016, **116**, 9438–9484.
34 Y. Wang, W. Liu, R. Guo, Q. Qu, H. Zheng, J. Zhang and Y. Huang, *J. Mater. Chem. A*, 2019, **7**, 22621–22630.
35 Q. Zhao, C. Guo, Y. Lu, L. Liu, J. Liang and J. Chen, *Ind. Eng. Chem. Res.*, 2016, **55**, 5795–5804.
36 Q. Zhao, Z. Zhu and J. Chen, *Adv. Mater.*, 2017, **29**, 1607007.
37 C. Gu, N. Huang, Y. Chen, H. Zhang, S. Zhang, F. Li, Y. Ma and D. Jiang, *Angew. Chem., Int. Ed.*, 2016, **55**, 3049–3053.
38 A. Banerjee, R. B. Araujo, M. Sjödin and R. Ahuja, *Nano Energy*, 2018, **47**, 301–308.
39 S. Maiti, A. Pramanik, T. Dhawa and S. Mahanty, *Mater. Lett.*, 2017, **209**, 613–617.
40 Y. Zhu, P. Chen, Y. Zhou, W. Nie and Y. Xu, *Electrochim. Acta*, 2019, **318**, 262–271.
41 Y. Song, Y. Gao, H. Rong, H. Wen, Y. Sha, H. Zhang, H. J. Liu and Q. Liu, *Sustainable Energy Fuels*, 2018, **2**, 803–810.
42 B. Zhang, Y. Zhang, X. Yang, G. Li, S. Zhang, Y. Zhang, D. Yu, Z. Liu and G. He, *Chem. Mater.*, 2020, **32**, 10575–10583.
43 Z. Wang, P. Zhang, J. Li, C. Zhang, J. X. Jiang, M. Lv, Z. Ding and B. Zhang, *Front. Chem.*, 2022, **10**, 1056244.
44 D. Chen, A. Avestro, Z. Chen, J. Sun, S. Wang, M. Xiao, Z. Erno, M. M. Algaradah, M. S. Nassar, K. Amine, Y. Meng and J. F. Stoddart, *Adv. Mater.*, 2015, **27**, 2907–2912.
45 M. Chen, C. Yang, Z. Xu, Y. Tang, J. Jiang, P. Liu, Y. Su and D. Wu, *RSC Adv.*, 2016, **6**, 13666–13669.
46 G. S. Vadehra, R. P. Maloney, M. A. Garcia-Garibay and B. Dunn, *Chem. Mater.*, 2014, **26**, 7151–7157.
47 M. Al Kobaisi, S. V. Bhosale, K. Latham, A. M. Raynor and S. V. Bhosale, *Chem. Rev.*, 2016, **116**, 11685–11796.
48 S. V. Bhosale, M. Al Kobaisi, R. W. Jadhav, P. P. Morajkar, L. A. Jones and S. George, *Chem. Soc. Rev.*, 2021, **50**, 9845–9998.
49 Y. Shi, Y. Lin, F. Kang, N. Aratani, W. Huang and Q. Zhang, *ACS Appl. Mater. Interfaces*, 2023, **15**, 1227–1233.
50 X. Liu and Z. Ye, *Adv. Energy Mater.*, 2020, **11**, 2003281.
51 Z. Chen, H. Su, P. Sun, P. Bai, J. Yang, M. Li, Y. Deng, Y. Liu, Y. Geng and Y. Xu, *Proc. Natl. Acad. Sci. U. S. A.*, 2022, **119**, e2116775119.
52 C. Han, H. Li, R. Shi, T. Zhang, J. Tong, J. Li and B. Li, *J. Mater. Chem. A*, 2019, **7**, 23378–23415.
53 T. Huang, D. Lu, L. Ma, X. Xi, R. Liu and D. Wu, *Chem. Eng. J.*, 2018, **349**, 66–71.
54 S. Hu, W. Zhang, J. Bai, G. Lu, L. Zhang and G. Wu, *RSC Adv.*, 2016, **6**, 25695–25702.
55 Y. Qin, Q. Peng, Y. Ding, Z. Lin, C. Wang, Y. Li, F. Xu, J. Li, Y. Yuan, X. He and Y. Li, *ACS Nano*, 2015, **9**, 8933–8941.

56 M. Seydou, J. Teyssandier, N. Battaglini, G. T. Kenfack, P. Lang, F. Tielens, F. Maurel and B. Diawara, *RSC Adv.*, 2014, **4**, 25698–25708.
57 A. B. Deshmukh, M. R. Biradar, M. D. Pawar, S. V. Bhosale and M. V. Shelke, *J. Energy Storage*, 2022, **56**, 106036.
58 L. Kortekaas, F. Lancia, J. D. Steen and W. R. Browne, *J. Phys. Chem. C*, 2017, **121**, 14688–14702.
59 G. Liu, L. Huang, Y. Wang, J. Tang, Y. Wang, M. Cheng, Y. Zhang, M. J. Kipper, L. A. Belfiore and W. S. Ranil, *RSC Adv.*, 2017, **7**, 49159–49165.
60 N. Kumar, T. A. Wani, P. K. Pathak, A. Bera and R. R. Salunkhe, *Sustainable Energy Fuels*, 2022, **6**, 1762–1769.
61 F. Ma, Z. Hu, L. Jiao, X. Wang, Y. Yang, Z. Li and Y. He, *Adv. Mater. Interfaces*, 2021, **8**, 2002161.
62 G. Sun, Y. Hu, Y. Sha, C. Shi, G. Yin, H. Zhang, H. J. Liu and Q. Liu, *Mater. Chem. Phys.*, 2019, **236**, 121815.
63 H. Zhang, Y. Fang, F. Yang, X. Liu and X. Lu, *Energy Environ. Sci.*, 2020, **13**, 2515–2523.
64 N. Kumar, N. Bansal, Y. Yamauchi and R. R. Salunkhe, *Chem. Mater.*, 2022, **34**, 4946–4954.
65 Y. Ding, F. Zhang, J. Xu, Y. Miao, Y. Yang, X. Liu and B. Xu, *RSC Adv.*, 2017, **7**, 28754–28762.
66 L. Chen, D. Zhao, S. Chen, X. Wang and C. Chen, *J. Colloid Interface Sci.*, 2016, **472**, 99–107.
67 S. Zhang, K. Zhu, Y. Gao, T. Bao, H. Wu and D. Cao, *Chem. – Asian J.*, 2023, **18**, e202300439.
68 B. Chang, J. Ma, T. Jiang, L. Gao, Y. Li, M. Zhou, Y. Huang and S. Han, *RSC Adv.*, 2020, **10**, 8729–8734.
69 M. Lv, F. Zhang, Y. Wu, M. Chen, C. Yao, J. Nan, D. Shu, R. Zeng, H. Zeng and S. L. Chou, *Sci. Rep.*, 2016, **6**, 23515.
70 B. Zhang, Y. Yu, Z. L. Xu, S. Abouali, M. Akbari, Y. B. He, F. Kang and J. K. Kim, *Adv. Energy Mater.*, 2014, **4**, 1301448.
71 J. D. Bagley, D. K. Kumar, K. A. See and N. C. Yeh, *RSC Adv.*, 2020, **10**, 39562–39571.
72 P. K. Pathak, V. P. Joshi, N. Kumar and R. R. Salunkhe, *Mater. Adv.*, 2022, **3**, 7235–7240.